

Double-exchange ferromagnetism of fermionic atoms in a *p*-orbital hexagonal lattice

Haoran Sun,¹ Erhai Zhao,² Youjin Deng,¹ and W. Vincent Liu^{3,*}

¹*Hefei National Research Center for Physical Sciences at the Microscale and School of Physical Sciences, University of Science and Technology of China, Hefei 230026, China*

²*Department of Physics and Astronomy, George Mason University, Fairfax, Virginia 22030, USA*

³*Department of Physics and Astronomy and IQ Initiative, University of Pittsburgh, Pittsburgh, Pennsylvania 15260, USA*

(Dated: January 29, 2026)

A large class of correlated quantum materials feature strong Hund’s coupling. Yet cold-atom quantum simulators have so far focused primarily on single-orbital Fermi-Hubbard systems near a Mott insulator. Here we show that repulsively interacting fermions loaded into the *p*-bands of a hexagonal lattice offer a unique platform to study the interplay of “Hundness” and “Mottness.” Our theory predicts that the orbital degrees of freedom, despite geometric frustration, produce a rich phase diagram featuring a competing itinerant ferromagnetic (FM) metal and a spin-1 antiferromagnetic (AFM) insulator, with a surprising first-order transition between them controlled by density near half-filling. Ferromagnetism emerges at low fillings from the flat band and persists to stronger interactions and higher fillings via a double-exchange mechanism, where spins align to avoid Hund-rule penalties at the expense of Dirac-fermion kinetic energy. We further argue that the paramagnetic regime is a correlated “Hund metal.” *p*-orbital Fermi gases thus provide an ideal experimental setting to investigate competing exchange mechanisms in multi-orbital systems with coexisting localized and itinerant spins.

In many correlated materials [1] such as cuprates, pnictides, and ruthenates, the *d*- or *f*-orbital degrees of freedom (DOF) play an active role in giving rise to a wealth of cooperative phenomena, ranging from orbital ordering, magnetism, to unconventional superconductivity [2, 3]. These interacting multi-orbital systems provide a natural arena for the interplay between two paradigms of strong correlation: “Mottness”, driven by on-site repulsion *U* which typically leads to antiferromagnetism via superexchange, and “Hundness”, driven by Hund’s rule coupling *J_H* which promotes high-spin states and itinerant ferromagnetism via mechanisms like double-exchange [4]. It remains a theoretical challenge to quantify the coexistence and competition of these two mechanisms, in part due to complications from crystal fields, phonons, or spin-orbit coupling. Ultracold atoms in optical lattices can serve as excellent quantum simulators to explore strong correlation physics, e.g., the Fermi-Hubbard model, in a simpler, cleaner, and highly tunable environment [5]. However, so far the experimental efforts have predominantly focused on the lowest *s*-orbital band [6], leaving the rich physics inherent in higher orbital bands [7], such as in *p*-bands dominated by Hund’s coupling, largely unexplored.

Some of the uniquely interesting properties of interacting atoms in the *p* band of optical lattices have been recognized before. A defining feature of *p*-orbitals is their spatial symmetry which leads to anisotropic hopping patterns distinct from the familiar *t_g* or *t_{2g}* orbitals found in many transition metal oxides and, as a result, gives rise to topologically nontrivial band structures in ladders [8] or flat bands on the hexagonal lattice [9]. In the Mott limit of strong interaction and integer filling, virtual hopping induces anisotropic kinetic exchange interactions. For

example, for spin-polarized *p*-orbital fermions, [10, 11] derived the orbital exchange Hamiltonian to show it is geometrically frustrated on many two-dimensional lattices, and [12] generalized the 120° model to a tripod model that also contains the Ising and Kitaev model at special limits. For (pseudo)spin 1/2 atoms, the *p*-orbital interaction Hamiltonian (Eq. 2) derived from the contact *s*-wave interaction between atoms of opposite spins differs from the Hubbard-Kanamori form characteristic of the Coulomb interaction between electrons in solids. For *p*-band fermions on the cubic lattice, it has been noted that the ferromagnetic and antiferromagnetic phases compete and are separated by a paramagnetic state [13]. There is a large body of work on bosonic atoms on higher orbital bands. For instance, spin-orbital intertwined order and exotic superfluid phases have been predicted for two-component bosons in hexagonal lattices [14].

In this work, we present a comprehensive analysis of interacting fermionic atoms on the *p*-band of hexagonal optical lattice, where the coexistence of flat band and dispersive Dirac cones, multi-orbital interactions, and Fermi statistics conspire to provide a fertile ground for competing orders. Previous studies have identified flat-band ferromagnetism (FM) at ultra low fillings [15] and a staggered antiferromagnetic (AFM) insulator [9] at half-filling. The physics beyond these two special limits has remained inconclusive and mysterious. It was conjectured that phase coexistence, orbital order, or even ferrimagnetic order are possible [9]. Our work is motivated to address the following open questions: What is the mechanism that stabilizes ferromagnetism when doping away from the half-filled AFM insulator? And what is the nature of the transition, if any, between the AFM insulator and FM metal?

Our analysis yields a few unexpected results. First, long-range orbital order is suppressed by geometric frustration on the hexagonal lattice, in sharp contrast to what happens on the square lattice [10, 16], so that the phase diagram is dominated by the competition between distinct spin orders. Second, the itinerant FM phase is robust and extends to higher fillings and strong interactions. The flat band provides a solid foundation to promote FM, but it is not exactly a prerequisite. Third, upon doping the AFM insulator, the FM phase is stabilized by the celebrated double-exchange mechanism, and is separated from AFM by a first-order phase transition. Throughout the FM phase, itinerant carriers coexist with localized moments, even though the underlying physics responsible for the localization is different in two limits: the localized states are associated with flat band at low filling, while spin-1 moments are formed due to “Mottness” near half filling. While all terms in the interaction Hamiltonian contribute, as we will explain below, the persistence of FM is largely due to Hund’s coupling.

To realize the double exchange mechanism, a cornerstone of magnetism in solids [17–19], has been a long-standing challenge for quantum simulators [20]. It is interesting that it emerges naturally in our setup. The FM-AFM transition is controlled solely by particle filling to constitute a novel route to control magnetism in *p*-orbital systems. Our results pinpoint the relevance of “Hundness” in orbital quantum gases and provide concrete theoretical predictions for current ultracold atom experiments [21–23].

Model Hamiltonian. We consider spin-1/2 fermions loaded in the *p*-bands of a hexagonal optical lattice, assuming the *s*-band below are completely filled and well separated from the *p*-bands. The system’s kinetics are described by a tight-binding Hamiltonian with nearest-neighbor hopping:

$$H_t = \sum_{\vec{r} \in A, i, \sigma} t_{\parallel} c_{i\sigma}^{\dagger}(\vec{r}) c_{i\sigma}(\vec{r} + \hat{e}_i) + \text{H.c.} \quad (1)$$

Here, $c_{i\sigma}(\vec{r})$ annihilates a fermion with spin σ at site \vec{r} with the *A* sublattice in an orbital projected to the direction of unit vector \hat{e}_i (as a superposition of p_x and p_y), t_{\parallel} is the longitudinal hopping amplitude (for details see Appendix). In typical experiments, transverse hopping is negligible, $t_{\perp} \ll t_{\parallel}$, and we set $t_{\parallel} \equiv t = 1$ as our energy unit. The validity of this approximation in H_t and the restriction to the *p*-orbital manifold rests on a clear hierarchy of energy scales found in typical optical lattice experiments, as detailed in Appendix . The resulting non-interacting band structure features two perfectly flat bands touching two dispersive bands with Dirac cones as shown in Fig. 1.

The interaction Hamiltonian is obtained by approximating the local optical potential, assumed deep, as a harmonic oscillator and decomposing the on-site *s*-wave

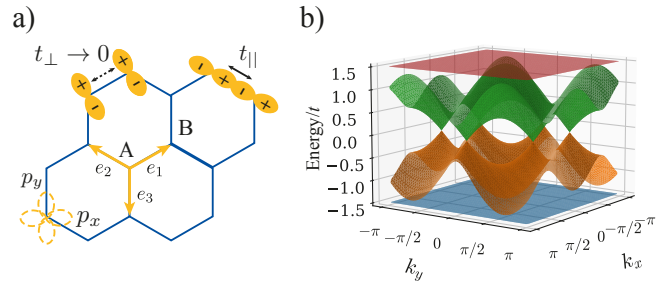


FIG. 1. (a) Schematic of the hexagonal lattice, showing the *A* and *B* sublattices and the nearest-neighbor vectors. Transverse hopping t_{\perp} is neglected. (b) The non-interacting band structure for $t_{\perp} = 0$, featuring two inequivalent Dirac cones and two perfectly flat bands at energies $\epsilon = \pm 3/2t$.

repulsion in the Wannier basis, and only keeping the *p*-orbital manifold [24, 25]:

$$H_{\text{int}} = \frac{3U}{4} (n_{x\uparrow}n_{x\downarrow} + n_{y\uparrow}n_{y\downarrow}) + \frac{U}{4} (n_{x\uparrow}n_{y\downarrow} + n_{y\uparrow}n_{x\downarrow}) + \frac{U}{4} (\Delta_x^{\dagger}\Delta_y + \Delta_y^{\dagger}\Delta_x - S_x^+S_y^- - S_y^+S_x^-) \quad (2)$$

where $n_{\mu\sigma} = c_{\mu\sigma}^{\dagger}c_{\mu\sigma}$ is the number operator, $\Delta_{\mu} = c_{\mu\downarrow}c_{\mu\uparrow}$ is the intra-orbital pair transfer operator, and $S_{\mu}^+ = c_{\mu\uparrow}^{\dagger}c_{\mu\downarrow}$ is the spin raising operator for orbital $\mu = x, y$. The interaction energy scale $U > 0$ is the on-site interaction for atoms in the *s*-orbital band. The Wannier functions for *p*-orbitals have smaller overlap, so the intra-orbital repulsion is $3U/4$ [24, 25]. The remaining terms are the inter-orbital repulsion, pair transfer, and Hund’s coupling (notice the sign), $-\frac{U}{4}(S_x^+S_y^- + S_y^+S_x^-)$, that favors spin alignment on the same site. The repulsion terms are foundational to Mott physics [6], while the Hund’s coupling is the primary driver of ferromagnetic spin correlations [4, 26]. This operator structure is generic for multi-orbital systems and is also found for Coulomb interactions, albeit with different prefactors [27].

We can rewrite H_{int} so that the competing orders become more transparent. Define the pseudo-spin operators $T_{\sigma}^j = \frac{1}{2} \sum_{\mu, \mu'} c_{\mu\sigma}^{\dagger} \tau_{\mu\mu'}^j c_{\mu'\sigma}$ (a vector in orbital space for each spin σ) and the spin operators $S_{\mu}^j = \frac{1}{2} \sum_{\sigma, \sigma'} c_{\mu\sigma}^{\dagger} \sigma_{\sigma\sigma'}^j c_{\mu\sigma'}$ (for each orbital μ), then [16]

$$H_{\text{int}} = -\frac{U}{2} \left[(T_{\uparrow}^y + T_{\downarrow}^y)^2 + (\vec{S}_x + \vec{S}_y)^2 \right] + \frac{U}{2} n. \quad (3)$$

where $n = \sum_{\mu\sigma} n_{\mu\sigma}$ is the total number operator. This form separates the interaction into spin and orbital channels and makes the SU(2) spin symmetry and SO(2) orbital rotation symmetry manifest. Spin ordering, driven by the total spin term $(\vec{S}_x + \vec{S}_y)^2$, will compete with orbital ordering, governed by the $(T_{\uparrow}^y + T_{\downarrow}^y)^2$ term. It is particularly amenable to field-theoretic analysis: the

squared operators can be decoupled by introducing auxiliary fields-a scalar field for the orbital channel and a vector field for the spin channel-via Hubbard-Stratonovich transformations [28].

Absence of orbital order. The full Hamiltonian $H_t + H_{int}$ for general values of U and filling fraction of the p -bands presents a formidable many-body problem. In this work, we limit our attention to a simple, yet unbiased and comprehensive, approximation scheme. As detailed in Appendix, we first express H_{int} in terms of (spin- and site-resolved) orbital pseudo-spin operators $T_{i,\sigma}^j$ and define order parameter $t_{i,\sigma}^j = \langle T_{i,\sigma}^j \rangle$, then decouple H_{int} into a quadratic mean-field Hamiltonian H_{MF} and solve $H_t + H_{MF}$ self-consistently with the number equation at zero temperature. We allow all possible spin and orbital wave configurations and do not assume a priori the (co-)existence or absence of any particular order. The resulting ground-state phase diagram in the chemical potential (μ) versus interaction (U) plane is presented in Fig. 2. Previous works only discussed certain limits of this global phase diagram, and our calculation serves as the prerequisite step toward understanding the intricate phases in this multi-orbital system.

The absence of long-range orbital order in Fig. 2 results from the competition between spin and orbital sectors inherent in the interaction Eq. 3. While the bipartite hexagonal lattice supports unfrustrated magnetic orders, the orbital channel is suppressed by strong geometric frustration. Unlike on the square lattice [16], the hexagonal geometry precludes simultaneous bond-energy minimization for orbitals (Fig. 3). Consequently, the frustrated orbital channel is energetically costly, ceding the ground state to the unfrustrated spin channel. This mechanism mirrors the frustration observed in p -orbital bosons [14] and spinless fermions [10, 11] on hexagonal lattice, where complex circulating orbital textures are predicted.

The stability against orbital ordering can be further confirmed by examining the collective orbital excitations over a postulated (e.g. FM or AFM) state. A field-theoretic calculation confirms that the orbital excitations are fully gapped throughout the phase diagram (see Appendix for details). The finite gap ensures that the system is not close to any instability toward orbital order. Consequently, the unfrustrated spin order prevails.

Kinetic exchange for spin-1. With orbital order suppressed, the phase diagram consists of a paramagnetic (PM) metal, a ferromagnetic (FM) metal, and a half-filled antiferromagnetic (AFM) insulator. At half-filling ($\langle n \rangle = 2$), for interactions U above a critical value U_c , the system undergoes a second-order transition from a semi-metal to an AFM insulator. This AFM phase is characterized by a non-zero staggered magnetization, m_s , which modulates the local density according to:

$$\langle n_{\alpha,\sigma} \rangle = 1 + \alpha\sigma m_s. \quad (4)$$

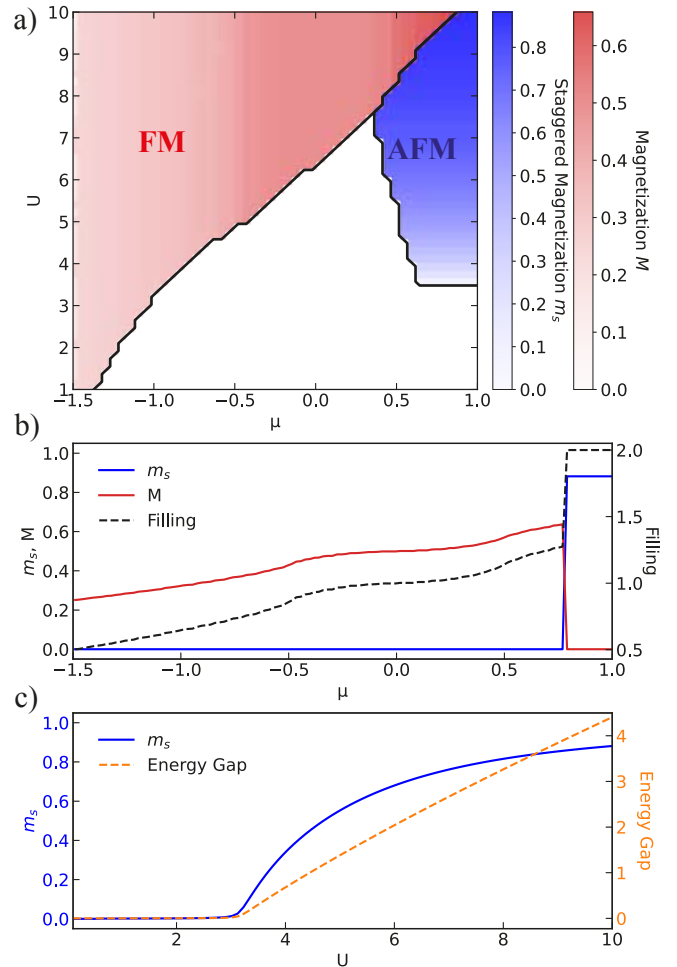


FIG. 2. Overview of spin order and phase competition. (a) Mean-field phase diagram in the μ - U plane (units: $t \equiv 1$). The color map shows the magnitude of the order parameter for the ferromagnetic (FM) phase (total magnetization M , red) and the antiferromagnetic (AFM) phase (staggered magnetization m_s , blue). The system exhibits a paramagnetic (PM) phase in the white region where both order parameters are zero. (b) A detailed slice at strong interaction $U = 10$, showing the order parameters (staggered magnetization m_s , blue line; total magnetization M , red line) and the total filling ($\langle n \rangle$) (black dashed line) as a function of chemical potential μ . The discontinuous jumps in m_s , M , and $\langle n \rangle$ signal a first-order phase transition between the FM and AFM states. (c) A slice at half-filling ($\langle n \rangle = 2$). The plot shows the staggered magnetization m_s (solid blue line) and the corresponding energy gap (dashed orange line) as a function of interaction strength U . The system undergoes a continuous, second-order phase transition into the AFM state at a critical interaction of $U_c \approx 3.253t$, where the energy gap opens.

Here, $\alpha = \pm 1$ for sublattices A/B and $\sigma = \pm 1$ for spin up/down, and the orbital index μ is implicitly summed over due to the absence of orbital order. Opening a Mott

gap at the Dirac points is described by

$$\frac{4}{U} = \frac{1}{\sqrt{9/4 + (Um_s)^2}} + \int d\epsilon \frac{g(\epsilon)}{\sqrt{\epsilon^2 + (Um_s)^2}}, \quad (5)$$

where $g(\epsilon)$ is the density of states of the Dirac bands. This yields a critical interaction strength of $U_c \approx 3.253t$.

As a signature of the interacting p -orbital system, this AFM phase differs from the familiar case of single-band Hubbard model. At half filling, each lattice site is occupied by two fermions, and strong onsite interactions H_{int} (specifically, the Hund's coupling) align their spins to form a local spin-1 complex [9]. To see the AFM order, consider virtual hopping processes induced by perturbation H_t . The dominant contribution comes from two parallel spins hopping to nearby site populated by two opposite spins, yielding an intermediate state with 4 spins on the same site, before hopping back. The picture is similar to the standard kinetic exchange, but for spin-1 complexes. Perturbation theory shows that the effective interaction J_{AFM} is antiferromagnetic and its magnitude scales as $J_{AFM} \sim 16t^4/U^3$. In this sense, it is a weaker antiferromagnet. As we shall see below, interesting things happen when it is doped by holes.

Beyond flat-band ferromagnetism. The emergence of ferromagnetic (FM) order at low fillings, $0.25 < n < 0.5$, and small U is triggered by the flat band inherent to p -orbitals on hexagonal lattice [15]. The flat band supports a set of degenerate, compact localized (“plaquette”) states and the FM order is a result of a direct exchange mechanism, mediated by the virtual hopping process between localized $1/2$ spins [9]. The on-site interaction Hamiltonian (Eq. 2) explicitly includes a Hund's rule coupling term, making the effective spin-spin interaction favors a spin-aligned state. This result is also in accordance with the Mielke-Tasaki theorem for flat-band ferromagnetism in Hubbard-like systems [29, 30].

For filling $n > 0.5$ and finite U , however, it is no longer sufficient to consider only the plaquette states or the flat band, because particles can be lifted by the interaction from the flat band into the dispersive lower Dirac band. Despite this, at small U and low filling, it is still useful to view the system self-organized into two parts: mobile carriers plus a ferromagnetic background of localized spins. Orbital induced Hund's coupling prefers a mobile carrier to align its spin with the FM background. In other words, interaction U stabilizes and promotes ferromagnetism. On the other hand, it costs kinetic energy for mobile carriers to occupy higher bands (instead of staying low with opposite spins).

Thus, for fixed U and increasing μ , as more and more carriers are added, the FM order will eventually becomes disfavored to give away to a paramagnetic metal (PM). Our calculation confirms this intuition and predicts a FM-PM phase boundary extending to large U and μ . The FM phase is characterized by its order parameter,

the magnetization M ,

$$M = \frac{1}{2N} \sum_{\vec{r}} \langle n_{\vec{r},\uparrow} \rangle - \langle n_{\vec{r},\downarrow} \rangle, \quad (6)$$

where N is the total number of sites. In Fig. 2(a) and (b), M only depends weakly on U but increases with μ . In particular, the m_s curve trails the filling. This agrees with the qualitative picture above that added carriers contribute to the magnetization. The robustness of FM order, well beyond the flat band regime studied before, is largely due to Hund's coupling.

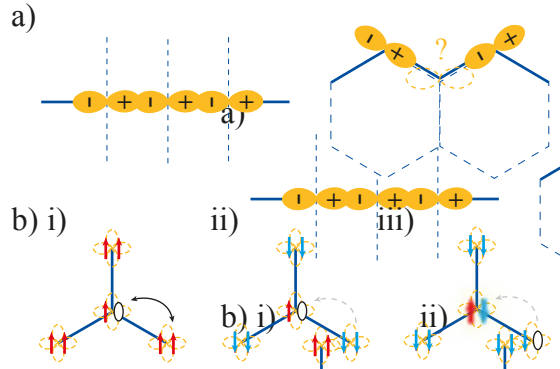


FIG. 3. Schematics of competing mechanisms governing the system's ground state. (a) Geometric orbital frustration on the hexagonal lattice. Unlike in square lattice where a simple ferro-orbital alignment is unfrustrated (left), the hexagonal geometry makes it impossible to simultaneously minimize the kinetic energy across all bonds due to p -orbital geometry (right). This conflict strongly suppresses the tendency towards long-range orbital order. (b) The double-exchange mechanism. (i) A FM background allows holes to delocalize freely. (ii) In AFM background, the hopping process is suppressed. (iii) Hopping is energetically penalized by a large on-site Hund's coupling, $J_H = U/4$ (blurred spins). This blockade of hopping in the AFM state makes the FM state energetically favored at finite doping.

Double-exchange-driven AFM-FM transition. In the unexplored regime near half fillings and strong U , the mechanism of flat-band ferromagnetism becomes irrelevant. To understand how hole doping drives an FM instability, consider a single hole introduced into the half-filled spin-1 AFM insulator. The remaining particle on the doped site ($\uparrow \circ$) occupies the flat band; consequently, it acts as a localized magnetic moment, mirroring the core electrons in transition metal magnets. As illustrated in Fig 3b(ii) and (iii), carrier transport in an AFM background is energetically suppressed: if an particle hops onto a hole-doped site ($\uparrow \circ$) from a neighbor with antiparallel spin ($\downarrow\downarrow$), the resulting doubly occupied site forms a low-spin ($S = 0$) state, violating Hund's rule and incurring an energy penalty $J_H = U/4$. As a result, the effective hopping of the hole is suppressed. In contrast,

a ferromagnetic background allows the itinerant carrier to hop to neighboring sites while maintaining the energetically favorable high-spin ($S = 1$) configuration, as shown in Fig 3b(i). This allows the holes to fully delocalize and maximize their kinetic energy gain. When this kinetic gain exceeds the cost of breaking the anti-ferromagnetic superexchange bonds, the itinerant carriers enforce ferromagnetic alignment on localized spins to optimize their mobility, and the system undergoes a first-order transition to the FM state. This process realizes the double-exchange mechanism [17–19], the fundamental driver of ferromagnetism in conductive transition metal oxides such as manganites and magnetite.

The direct FM-to-AFM transition occurs when the kinetic energy gain from hole delocalization in the FM state, ΔE_{FM} , is comparable to the interaction energy gain by developing antiferromagnetic order, $\Delta E_{AFM} \propto J_{AFM}(1 - \delta)^2$. For small hole doping $\delta = 2 - \langle n \rangle$, the kinetic energy of the metallic FM phase can be computed from the linear density of states of the Dirac bands, $\Delta E_{FM} \propto t\delta^{3/2}$. Equating ΔE_{FM} to ΔE_{AFM} yields the scaling of the AFM-FM phase boundary in terms of critical doping $\delta_c \propto (t/U)^2$. The trend agrees with the self-consistent mean field result in Fig. 2. In particular, as $U \rightarrow \infty$, the AFM becomes unstable at infinitesimal hole doping. This serves yet another testimony to the robustness of FM. The direct transition stands in sharp contrast to standard models, where transitions between distinct magnetic orders often require changing the sign of the exchange coupling from antiferromagnetic to ferromagnetic.

We emphasize that the landscape of competing magnetic orders shown in Fig. 2 is a direct consequence of the orbital degree of freedom. The standard s -band Hubbard model on the hexagonal lattice does not host a stable itinerant FM phase; it only exhibits a transition from a paramagnetic metal to an AFM insulator [31–33]. It is interesting that in our system, depending on the filling and interaction strength, three different mechanisms are at play: flat-band ferromagnetism, kinetic exchange for spin-1 AFM, and double-exchange. Throughout, Hund's coupling that favors spin-aligned configurations plays an important role.

We establish that interacting fermions in the p -orbitals of a hexagonal lattice open not only a natural platform for quantum simulating double exchange, a cornerstone of magnetism in solids [17, 18], but also access to a previously unexplored parameter regime beyond standard condensed-matter settings. In our system localized moments and itinerant carriers emerge intrinsically from the flat and dispersive Dirac bands, which overcomes the long-standing challenge of engineering double exchange with cold atoms [34]. The orbital degree of freedom further generates pronounced Hund physics, yielding a robust ferromagnetic phase and a filling-driven FM-AFM transition. Although geometric frustration suppresses

long-range orbital order, the orbitals remain essential; unlike in the single-band Hubbard model, Hund's coupling in Eq. 2 reshapes the spin sector by stabilizing itinerant ferromagnetism at low fillings and forming local spin-1 units that underpin the antiferromagnetic state at half filling [26].

These predictions are directly testable with current ultracold-atom techniques for manipulating orbital states and tuning interactions in optical lattices [5, 21]. The distinct phases, from staggered order to double-exchange-driven ferromagnetism, can be identified with time-of-flight imaging, momentum-resolved spectroscopy, and *in-situ* microscopy [35, 36]. This study lays the groundwork for incorporating quantum fluctuations using numerical methods such as DMFT or QMC [37, 38]. It may shed further light on the paramagnetic metal, which is suspected to be a Hund metal with non-Fermi liquid properties near the FM or AFM transition and to develop other many-body instabilities such as unconventional superfluidity.

Acknowledgments The authors gratefully acknowledge helpful discussions with Andreas Hemmerich, Xiaopeng Li, and Peter Zoller. This work is supported by the National Natural Science Foundation of China (NSFC) under Grant No. 12204173 and No. 12275263, the Innovation Program for Quantum Science and Technology under Grant No. 2021ZD0301900 (H.S. and Y.D.), and the AFOSR Grant No. FA9550-23-1-0598 (E.Z. and W.V.L.).

* wvliu@pitt.edu

- [1] Y. Tokura and N. Nagaosa, *Science* **288**, 462 (2000).
- [2] F. C. Zhang, *Physical Review B* **37**, 3759 (1988).
- [3] W. Chen, C. Neerup Breiø, F. Massee, M. P. Allan, C. Petrovic, J. C. S. Davis, P. J. Hirschfeld, B. M. Andersen, and A. Kreisel, *Nature Communications* **14**, 2984 (2023).
- [4] K. M. Stadler, G. Kotliar, A. Weichselbaum, and J. von Delft, *Annals of Physics* **405**, 365 (2019).
- [5] I. Bloch, J. Dalibard, and W. Zwerger, *Rev. Mod. Phys.* **80**, 885 (2008).
- [6] M. Imada, A. Fujimori, and Y. Tokura, *Rev. Mod. Phys.* **70**, 1039 (1998).
- [7] X. Li and W. V. Liu, *Rep. Prog. Phys.* (2016).
- [8] X. Li, E. Zhao, and W. Vincent Liu, *Nature Communications* **4**, 1523 (2013).
- [9] S. Zhang, H.-h. Hung, and C. Wu, *Physical Review A* **82**, 053618 (2010).
- [10] E. Zhao and W. V. Liu, *Phys. Rev. Lett.* **100**, 160403 (2008).
- [11] C. Wu, *Phys. Rev. Lett.* **100**, 200406 (2008).
- [12] H. Zou, B. Liu, E. Zhao, and W. V. Liu, *New Journal of Physics* **18**, 053040 (2016).
- [13] L. Wang, *Physical Review A* **78** (2008).
- [14] Y. Li, J. Yuan, X. Zhou, and X. Li, *Physical Review Research* **3**, 033274 (2021).
- [15] C. Wu, D. Bergman, L. Balents, and S. Das Sarma, *Phys.*

Rev. Lett. **99**, 070401 (2007).

[16] Z. Zhou, E. Zhao, and W. V. Liu, Phys. Rev. Lett. **114**, 100406 (2015).

[17] C. Zener, Physical Review **82**, 403 (1951).

[18] P. W. Anderson, Physical Review **100**, 675 (1955).

[19] E. Koch, Correlated electrons: from models to materials **2** (2012).

[20] P. O. Bugnion and G. J. Conduit, Phys. Rev. A **88**, 013601 (2013).

[21] G. Wirth, M. Olschlager, and A. Hemmerich, Nature Physics **7**, 147 (2011).

[22] P. Soltan-Panahi, D.-S. Lümann, J. Struck, P. Windpassinger, and K. Sengstock, Nature Physics **8**, 71 (2012).

[23] S. Jin, X. Chen, and X. Zhou, Frontiers in Physics **10**, 957151 (2022).

[24] W. V. Liu and C. Wu, Physical Review A **74**, 013607 (2006).

[25] A. Isacsson and S. M. Girvin, Phys. Rev. A **72**, 053604 (2005).

[26] A. Georges, L. d. Medici, and J. Mravlje, Annual Review of Condensed Matter Physics **4**, 137 (2013).

[27] P. Fazekas, Lecture notes on electron correlation and magnetism (1999).

[28] Z. Koinov, Physica C: Superconductivity **470**, 144 (2010).

[29] A. Mielke and H. Tasaki, Communications in Mathematical Physics **158**, 341 (1993).

[30] R. Pons, A. Mielke, and T. Stauber, Physical Review B **102**, 235101 (2020).

[31] M. Raczkowski, R. Peters, T. T. Phùng, N. Takemori, F. F. Assaad, A. Honecker, and J. Vahedi, Physical Review B **101**, 125103 (2020).

[32] J. Ostmeyer, E. Berkowitz, S. Krieg, T. A. Lähde, T. Luu, and C. Urbach, Physical Review B **102**, 245105 (2020).

[33] M.-H. Zeng, Y.-J. Wang, and T. Ma, Phys. Rev. B **105**, 035155 (2022).

[34] M. Lewenstein, A. Sanpera, V. Ahufinger, B. Damski, A. S. De, and U. Sen, Advances in Physics **56**, 243 (2007).

[35] W. S. Bakr, J. I. Gillen, A. Peng, S. Fölling, and M. Greiner, Nature **462**, 74 (2009).

[36] J. F. Sherson, C. Weitenberg, M. Endres, M. Cheneau, I. Bloch, and S. Kuhr, Nature **467**, 68 (2010).

[37] A. Georges, G. Kotliar, W. Krauth, and M. J. Rozenberg, Rev. Mod. Phys. **68**, 13 (1996).

[38] K. Van Houcke, F. Werner, E. Kozik, N. Prokof'ev, B. Svistunov, M. J. H. Ku, A. T. Sommer, L. W. Cheuk, A. Schirotzek, and M. W. Zwierlein, Nature Physics **8**, 366 (2012).

[39] D. Jaksch, C. Bruder, J. Cirac, C. Gardiner, and P. Zoller, Phys. Rev. Lett. **81**, 3108 (1998).

Orbital Projection along Hopping Directions

The kinetic term in the Hamiltonian, Eq. (1), is expressed in a basis that rotates with the lattice bond direction. This is achieved by projecting the operators for the site-fixed Cartesian orbitals, $\{c_x, c_y\}$, onto axes parallel and perpendicular to the bond vectors.

The hopping term connects sites on sublattice A with neighboring sites on sublattice B. The unit vectors for

the longitudinal hopping (t_{\parallel}) term are:

$$\hat{e}_{1,2} = \pm \frac{\sqrt{3}}{2} \hat{x} + \frac{1}{2} \hat{y}, \quad \hat{e}_3 = -\hat{y}. \quad (\text{A1})$$

The operators $c_{\vec{r},i,\sigma}$ annihilate a fermion in an orbital oriented along the corresponding bond direction \hat{e}_i . They are defined as the projection of the Cartesian orbital operators:

$$c_i = (\hat{c}_x \hat{x} + \hat{c}_y \hat{y}) \cdot \hat{e}_i. \quad (\text{A2})$$

where \hat{x}, \hat{y} are unit vectors in corresponding directions. Similarly, the neglected transverse hopping term

$$H_{\perp} = \sum_{\vec{r} \in A, i, \sigma} t_{\perp} \tilde{c}_{i\sigma}^{\dagger}(\vec{r}) \tilde{c}_{i\sigma}(\vec{r} + \hat{e}_i) \quad (\text{A3})$$

is formulated by operator $\tilde{c}_{i\sigma}(\vec{r})$ corresponds to an orbital oriented perpendicular to the bond direction. The rotated unit vectors, \tilde{e}'_i , can be obtained by a $\pi/2$ counter-clockwise rotation of the unit vectors, $\hat{e}'_i = R(\pi/2)\hat{e}_i$. This gives $\hat{e}'_{1,2} = -\frac{1}{2}\hat{x} \pm \frac{\sqrt{3}}{2}\hat{y}$, $\hat{e}'_3 = \hat{x}$. The transverse hopping operators are the projection onto these rotated directions. This formulation captures the anisotropic nature of the p-orbital wavefunctions, where the hopping integral's value is determined by the relative orientation of the orbitals and the bond connecting them.

The single-particle spectrum derived from the free Hamiltonian with $t_{\perp} = 0$ consists of two flat bands at energies $\epsilon_{\text{flat}} = \pm \frac{3}{2}$ and two dispersive Dirac bands. The dispersion of the latter is given by

$$\epsilon(\vec{k}) = \pm \left[\frac{3}{2} + \cos(\sqrt{3}k_x) + 2 \cos\left(\frac{1}{2}k_y\right) \cos\left(\frac{\sqrt{3}}{2}k_x\right) \right]^{1/2}, \quad (\text{A4})$$

which are symmetric about the zero-energy plane, as illustrated in Fig. 1(b).

Experimental Realization and Energy Scales

The validity of our theoretical framework, which is confined to the p-orbital manifold and neglects transverse hopping ($t_{\perp} = 0$), rests on a specific hierarchy of energy scales that is naturally realized in ultracold atom experiments [21, 22]. This hierarchy is given by

$$\Delta_{sp} \gg U \sim t_{\parallel} \gg t_{\perp} \sim t_s, \quad (\text{A5})$$

where Δ_{sp} is the energy gap between the s- and p-orbital bands and t_s is the s-orbital hopping. These energy scales are tunable functions of the optical lattice depth V , usually expressed in units of the recoil energy $E_R = \hbar^2 k_L^2 / (2m)$, where $k_L = 2\pi/\lambda$ is the laser wavevector. In the deep lattice limit, the s-p band gap

arises from the harmonic confinement at the bottom of each potential well, scaling as $\Delta_{sp} \propto \sqrt{VE_R}$. In contrast, the tunneling amplitudes are exponentially suppressed, with $t_s \propto (V/E_R)^{3/4} \exp(-2\sqrt{V/E_R})$ [39]. A key feature of p-orbital systems is that the transverse hopping t_\perp has the same functional dependence and magnitude as the s-orbital hopping t_s , while the longitudinal hopping is significantly larger, scaling roughly as $t_\parallel \propto (\frac{\pi^2}{2} \sqrt{V/E_R}) t_s$ [25]. The interaction strength U depends on the s-wave scattering length a_s and scales as $U \propto (k_L a_s)(V/E_R)^{3/4}$ [39].

To provide a concrete example, a typical and easily realizable experimental setup with ^{40}K atoms at a lattice depth of $V = 12E_R$ and a tuned scattering length $a_s = 500a_0$ yields the ratios $U/t_\parallel \approx 9.4$ and $t_\parallel/t_\perp \approx 12$. Crucially, the s-p gap remains the largest scale, with $\Delta_{sp}/U \approx 4.3$. This demonstrates that even in the strongly correlated regime where interactions U dominate over the kinetic energy t_\parallel , the system is well-protected from correlation with the s-orbital band, firmly validating our p-orbital only model. Furthermore, these parameters are extremely tunable in optical lattice systems, making the rich physics we describe highly experimentally accessible.

Stability Against Orbital Ordering

A central claim in the main text is that the hexagonal lattice geometry frustrates and suppresses long-range orbital order. To substantiate this, we perform a field-theoretic analysis of the collective orbital excitations. We show that these excitations remain gapped throughout the physically relevant phases, indicating stability against an orbital ordering instability.

We begin with the on-site interaction Hamiltonian, expressed in terms of spin and orbital operators as given in Eq. (3) of the main text. This form is particularly amenable to a Hubbard-Stratonovich decoupling. We introduce auxiliary bosonic fields: a scalar field $\theta(\tau, \vec{r})$ coupling to the orbital channel ($T_\uparrow^y + T_\downarrow^y$), and a vector field $\vec{\phi}(\tau, \vec{r})$ coupling to the spin channel ($\vec{S}_x + \vec{S}_y$). Dropping the constant term $\frac{U}{2}n$, the effective action is:

$$S_{\text{eff}}[\vec{\phi}, \theta] = - \int d\tau \left(\frac{1}{2}\theta^2 + \frac{1}{2}|\vec{\phi}|^2 \right) - \text{Tr} \ln G^{-1}[\vec{\phi}, \theta], \quad (\text{A6})$$

where $G^{-1} = \partial_\tau - H_0 - M(\vec{\phi}, \theta)$ is the inverse Green's function for the fermions. H_0 is the non-interacting Hamiltonian and M represents the mean-field coupling.

We analyze the stability of the system by examining the fluctuations around the magnetic saddle point. We expand the action around the configuration determined by the self-consistent mean-field solution:

$$\vec{\phi}_c = \phi_z(-1)^\alpha \hat{z}, \quad \theta_c = 0. \quad (\text{A7})$$

Here, α is the sublattice index. The vanishing orbital expectation value $\theta_c = 0$ is the result of the mean-field energy minimization, consistent with the suppression of orbital order.

The inverse Green's function for the fermions in this background $\vec{\phi}_c$, written in the sublattice basis $\Psi(\vec{k}) = (c_{\mu\sigma A}(\vec{k}), c_{\mu\sigma B}(\vec{k}))^T$, is:

$$G_c^{-1}(k) = \omega - H_t(\vec{k}) \otimes I_{\text{spin}} - \phi_z I_{\text{orb}} \otimes \sigma_{\text{spin}}^z \otimes \sigma_{\text{site}}^z. \quad (\text{A8})$$

Expanding the action to second order in the orbital fluctuations $\theta(\vec{p}, \Omega)$ (where θ now denotes the fluctuation field around $\theta_c = 0$) yields:

$$S_\theta^{(2)}[\theta] = \frac{1}{2} \int \frac{d^2 p}{(2\pi)^2} \frac{d\Omega}{2\pi} |\theta(\vec{p}, \Omega)|^2 K_\theta(\vec{p}, \Omega; \phi_z), \quad (\text{A9})$$

where $K_\theta(\vec{p}, \Omega; \phi_z)$ is the inverse orbital propagator. Physically, it quantifies the energy stiffness against orbital fluctuations. A magnetic phase is stable against orbital ordering if the static stiffness $K_\theta(\vec{p} \rightarrow 0, \Omega \rightarrow 0)$ is strictly positive (indicating a massive, gapped mode), while a vanishing kernel would signal a divergence in susceptibility and an instability toward an ordered state.

In the static, long-wavelength limit ($\vec{p} \rightarrow 0, \Omega = 0$), the kernel takes the standard one-loop form:

$$K_\theta(0, 0; \phi_z) = 1 - \frac{iU}{4} \int \frac{d^2 k}{(2\pi)^2} \int \frac{d\omega}{2\pi} f(\vec{k}, \omega; \phi_z). \quad (\text{A10})$$

Here, the integral term represents the static polarization bubble (particle-hole susceptibility), with $f(\vec{k}, \omega; \phi_z)$ defined from the trace over the fermion Green's function loop:

$$f(\vec{k}, \omega; \phi_z) = \text{Tr} \left[G_c(\vec{k}, \omega; \phi_z) \Gamma_\theta G_c(\vec{k}, \omega; \phi_z) \Gamma_\theta \right],$$

where the vertex $\Gamma_\theta = \tau_{\text{orb}}^y \otimes I_{\text{spin}} \otimes I_{\text{site}}$ describes the coupling of the orbital field to the fermions.

For the semi-metallic phase where $\phi_z = 0$, numerical evaluation of the integral yields:

$$K_\theta(0, 0; 0) \approx 1 - \frac{iU}{4} (96.43i) = 1 + 24.1U. \quad (\text{A11})$$

This result is positive definite for all repulsive interactions $U > 0$. This implies that the static orbital susceptibility is finite and non-divergent.

For the AFM phase where $\phi_z > 0$, the structure of the kernel $K_\theta(0, 0; \phi_z)$ remains formally identical. We evaluate this kernel numerically as a function of the magnetic order parameter ϕ_z . As shown in Fig. A1, the kernel K_θ remains strictly positive throughout the transition from the semi-metal to the AFM insulator. Since the condition for a gapless mode (an instability) is $K_\theta(0, 0) \leq 0$, our result $K_\theta > 0$ confirms that the orbital excitations remain massive (gapped) across the phase diagram. This

provides robust field-theoretic evidence that the system is stable against spontaneous orbital ordering, justifying our treatment of the orbital degree of freedom as a un-ordered channel.

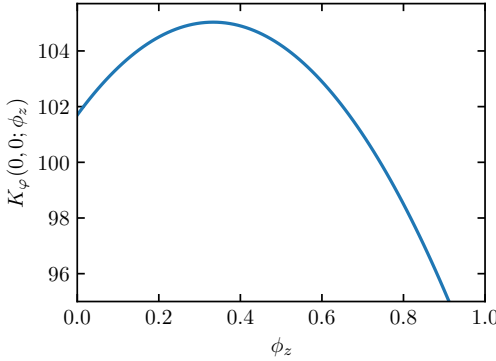


FIG. A1. The orbital stiffness kernel $K_\theta(0,0;\phi_z)$ as a function of the staggered magnetization field amplitude ϕ_z . The kernel remains positive definite across the entire range from the semi-metallic phase ($\phi_z = 0$) to the gapped AFM phase ($\phi_z > 0$). A positive value corresponds to a finite mass for the orbital fluctuations, indicating that the orbital excitations are gapped and the system is stable against orbital ordering.

Mean-Field Calculation Details

The ground-state phase diagrams were determined using a self-consistent mean-field theory. For this calculation, the on-site interaction Hamiltonian H_{int} is expressed using the orbital pseudo-spin operators $T_\sigma^j = \frac{1}{2} \sum_{\mu,\mu'} c_{\mu\sigma}^\dagger \tau_{\mu\mu'}^j c_{\mu'\sigma}$:

$$H_{\text{int}} = \frac{U}{2} T_{\uparrow}^0 T_{\downarrow}^0 + \frac{U}{4} T_{\uparrow}^x T_{\downarrow}^x + \frac{U}{4} T_{\uparrow}^z T_{\downarrow}^z. \quad (\text{A12})$$

Note that this expression is exactly equivalent to the form presented in Eq. (3) in the main text. Applying this decoupling to Eq. (A12) results in a quadratic mean-field Hamiltonian $H_{MF} = H_t + \sum_i H_{int,i}^{MF}$. The local interaction term, written explicitly in terms of the order parameters $t_{i,\sigma}^j = \langle T_{i,\sigma}^j \rangle$, is:

$$\begin{aligned} H_{int,i}^{MF} = & \frac{U}{2} (t_{i,\downarrow}^0 T_{i,\uparrow}^0 + t_{i,\uparrow}^0 T_{i,\downarrow}^0) \\ & + \frac{U}{4} (t_{i,\downarrow}^x T_{i,\uparrow}^x + t_{i,\uparrow}^x T_{i,\downarrow}^x) \\ & + \frac{U}{4} (t_{i,\downarrow}^z T_{i,\uparrow}^z + t_{i,\uparrow}^z T_{i,\downarrow}^z) - E_{\text{sub},i}, \end{aligned} \quad (\text{A13})$$

where $E_{\text{sub},i} = \frac{U}{2} t_{i,\uparrow}^0 t_{i,\downarrow}^0 + \frac{U}{4} t_{i,\uparrow}^x t_{i,\downarrow}^x + \frac{U}{4} t_{i,\uparrow}^z t_{i,\downarrow}^z$ is the standard double-counting correction. The full Hamiltonian H_{MF} is then solved self-consistently by diagonalizing it to find the new ground state expectation values $\langle T_{i,\sigma}^j \rangle$

until convergence is reached.

To ensure the robustness of our findings, we employed both momentum-space and real-space methods. First, we performed an unbiased search for the dominant ordering patterns in momentum space. The site-dependent order parameters were Fourier transformed, $t_{\alpha,\sigma}^j(\vec{q}) = \frac{1}{\sqrt{N}} \sum_{i \in \alpha} e^{-i\vec{q} \cdot \vec{r}_i} t_{i,\sigma}^j$, where $\alpha \in \{A, B\}$ is the sublattice index. In our initial calculation, the Fourier components $t_{\alpha,\sigma}^j(\vec{q})$ were treated as free parameters for all wavevectors \vec{q} in the Brillouin zone. This comprehensive search consistently found that the self-consistent solution minimized the energy only when $t_{\alpha,\sigma}^j(\vec{q})$ was non-zero for the uniform mode ($\vec{q} = 0$, ferromagnetic) or the staggered mode ($\vec{q} = K$, antiferromagnetic). To corroborate this, a complementary real-space calculation was performed on a finite diamond-shaped cluster (characteristic length of 21 sites), which, after iterating from numerous random initial states, confirmed the stability of only these FM and AFM phases. Then, having established the nature of the competing ground states, we mapped out the detailed phase diagrams using a simplified and computationally efficient model, where the self-consistent calculation was restricted to the subspace of order parameters with only $\vec{q} = 0$ or $\vec{q} = K$ components, which yielded the magnetic phase diagram presented in Fig. 2.

Derivation of the Antiferromagnetic Gap Equation

The onset of the staggered antiferromagnetic (AFM) phase at half-filling is described by a gap equation for the order parameter m_s . With the order parameter defined as in Eq. (4), the gap equation is cast as:

$$\frac{4}{U} = \int_{\text{BZ}} d^2k \frac{3\sqrt{3}}{8\pi^2} \frac{1}{\sqrt{\epsilon(\vec{k})^2 + (Um_s)^2}} + \frac{1}{\sqrt{\frac{9}{4} + (Um_s)^2}}, \quad (\text{A14})$$

which can be rewritten in terms of the density of states of the Dirac bands, $g(\epsilon)$, as

$$\frac{4}{U} = \frac{1}{\sqrt{\frac{9}{4} + (Um_s)^2}} + \int d\epsilon \frac{g(\epsilon)}{\sqrt{\epsilon^2 + (Um_s)^2}}.$$

To determine the critical interaction strength U_c for the onset of staggered magnetization, we analyze the gap equation in the limit $m_s \rightarrow 0$:

$$\frac{4}{U_c} = \frac{3\sqrt{3}}{4\pi^2} \int_{\text{BZ}} \frac{d^2k}{|\epsilon(\vec{k})|} + \frac{2}{3}, \quad (\text{A15})$$

where the integral accounts for the Dirac bands and the constant term arises from the flat bands. A precise numerical evaluation of the integral yields the critical interaction strength $U_c \approx 3.253t$. This result is independently confirmed by our full self-consistent mean-field calculations.